

Propagation of Spontaneously Actuated Pulsive Vibration in Human Heart Wall and In Vivo Viscoelasticity Estimation

Hiroshi Kanai,

Abstract—Though myocardial viscoelasticity is essential in the evaluation of heart diastolic properties, it has never been noninvasively measured in vivo. By the ultrasonic measurement of the myocardial motion, we have already found that some pulsive waves are spontaneously excited by aortic-valve closure (AVC) at end-systole (T_0). These waves may serve as an ideal source of the intrinsic heart sound caused by AVC. In this study, using a sparse sector scan, in which the beam directions are restricted to about 16, the pulsive waves were measured almost simultaneously at about 160 points set along the heart wall at a sufficiently high frame rate. The consecutive spatial phase distributions, obtained by the Fourier transform of the measured waves, clearly revealed wave propagation along the heart wall for the first time. The propagation time of the wave along the heart wall is very small (namely, several milliseconds) and cannot be measured by conventional equipment. Based on this phenomenon, we developed a means to measure the myocardial viscoelasticity in vivo. In this measurement, the phase velocity of the wave is determined for each frequency component. By comparing the dispersion of the phase velocity with the theoretical one of the Lamb wave (the plate flexural wave), which propagates along the viscoelastic plate (heart wall) immersed in blood, the instantaneous viscoelasticity is determined noninvasively. This is the first report of such noninvasive determination. In vivo experiments applied to five healthy subjects, propagation of the pulsive wave was clearly visible in all subjects. For the 60-Hz component, the typical propagation speed rapidly decreased from 5 m/s just before the time of AVC ($t = T_0 - 8$ ms) to 3 m/s at $t = T_0 + 10$ ms. In the experiments, it was possible to determine the viscosity more precisely than the elasticity. The typical value of elasticity was about 24–30 kPa and did not change around the time of AVC. The typical transient values of viscosity decreased rapidly from 400 Pa·s at $t = T_0 - 8$ ms to 70 Pa·s at $t = T_0 + 10$ ms. The measured shear elasticity and viscosity in this study are comparable to those obtained for the human tissues using audio frequency in in vitro experiments reported in the literature.

I. INTRODUCTION

FOR tissue characterization, shear waves are artificially actuated in tissues or phantoms to determine their

Manuscript received May 15, 2004; accepted April 25, 2005. This work was partly supported by grants-in-aid for scientific research from the Ministry, Education, Culture, Sports, Science, and Technology of Japan (2003–2004, No. 15300177, 2004–2005, No. 16650120, and 2005–2007, No. 17206043.).

The author is with the Department of Electronic Engineering, Graduate School of Engineering, Tohoku University, Sendai 980-8579, Japan (e-mail: hkanai@ecei.tohoku.ac.jp).

propagation speed and viscoelasticity [1]–[7]. However, spontaneously actuated vibrations propagating in the heart wall, which differ from electrically excited waves [8]–[10], have not been recognized at all. This is understandable given that the actual wave that propagates along the heart wall is minute (namely, only several tenths of a millimeter) and that the delay time from the base to the apex of the heart is very small, only several milliseconds.

Conventional ultrasonography, computer tomography (CT) [11], and magnetic resonant imaging (MRI) [12], [13] enable clinical visualization of cross-sectional images of the human heart, but their imaging is restricted to large motion (> 1 mm) and low-frequency components (< 30 Hz). Analysis of the motion-mode (M-mode) image [14], [15] is a candidate for transthoracic measurement of the minute and rapid heart-wall motion. However, the detectable amplitude is greater than the wavelength, which is equal to $411 \mu\text{m}$ for ultrasound with a frequency of 3.75 MHz normally applied to the heart in the clinical setting. Even when a higher frequency of 10 MHz is used, the wavelength and the detectable amplitude are still $154 \mu\text{m}$.

The tissue Doppler imaging (TDI) technique [16]–[21]—modified ultrasound two-dimensional (2-D) color flow mapping—enables determination of motion distribution of the myocardium in real time. Even in current measurement, however, the sampling frequency of the motion of the heart wall is low (at most 200 Hz [21]), that is, the sampling period is 5 ms, which is too long to detect the propagation time of the wave. Moreover, frequency analysis such as the Fourier transform has not been applied to the measured motion signal to detect the phase components.

To measure the original vibrations of the heart sounds (which are audible by stethoscope) using ultrasound from the chest wall, we have already developed a method to transcutaneously measure the heart-wall vibrations as a waveform at one point or multiple points preset along an ultrasonic beam in the heart wall [22], [23]. We found that there is a steep dip in the pulse that occurs exactly at the time of AVC (T_0) [24]. This notch also has been measured by the TDI approach with a commercial scanner to determine the time of AVC (T_0) [25].

Moreover, we have developed a method to measure the vibrations simultaneously at about 160 points preset in the heart wall [24]. In [24], it was revealed that there is a short delay of several milliseconds in the excitation of the steep dip of the notch pulse from the base to the apex of the

heart along the interventricular septum (IVS). However, no propagation phenomenon of the notch pulse along the heart wall was recognized in the previous report [24].

The use of the sparse sector scan has allowed us to simultaneously measure heart-wall motion at 160 points at a sufficiently high frame rate to measure the propagation of the notch pulse along the IVS. Therefore, from consecutively obtained spatial distributions of the phase value of the vibration wave, the present study reveals for the first time that the steep dip of the notch pulse, excited exactly at the time of AVC (T_0), propagates along the IVS from the base to the apex, and its phase velocity is determined. By analyzing various frequency components up to 90 Hz, the propagation speed shows the frequency dispersion. This dispersion characteristic agrees with the theoretical one of the Lamb wave that propagates in the viscoelastic plate immersed in fluid. By introducing the single Voigt model into the equation of the Lamb wave and fitting the derived theoretical phase velocity to the measured dispersion, the myocardial viscoelastic properties were determined noninvasively for the first time. The shear elastic and viscosity values in the *in vivo* experiments are comparable to those already obtained for human soft tissue in *in vitro* experiments for a similar audible frequency range as reported in the literature. This method offers potential for *in vivo* myocardial tissue characterization of diastolic properties, which cannot be obtained by conventional echocardiography, TDI, CT, or MRI.

II. IN VIVO EXPERIMENTAL RESULTS FOR EXAMINING POTENTIAL MATHEMATICAL MODEL

Fig. 1(a) shows a typical cross-sectional image (the transthoracic parasternal longitudinal-axis view) of a heart obtained by conventional echocardiography for a healthy young subject (subject A, 21 years old). The upper-right inset shows the scanning range of the ultrasonic beams in this imaging. From the conventional motion picture of Fig. 1(a), in our experience the human eye can detect motion only larger than 1 mm and slower than 1/30 second. The recognized slow motion also includes the lateral motion from the base to the apex during systole, the direction of which is perpendicular to the ultrasonic beam. However, for a short period of about 70 ms, it can be assumed that each point preset in the heart wall stays in the same focal area of each ultrasonic beam. This assumption was used in this study.

We previously developed an ultrasound-based transthoracic method (phased tracking method) to directly measure the heart wall vibrations [22], [23], [26]. Radio frequency (RF) pulses are transmitted from an ultrasonic transducer at a pulse repetition interval ΔT , and the reflected ultrasonic wave is received by the same transducer and quadrature demodulated. The time-domain complex cross-correlation technique is applied to determine the phase shift between the consecutively obtained resultant

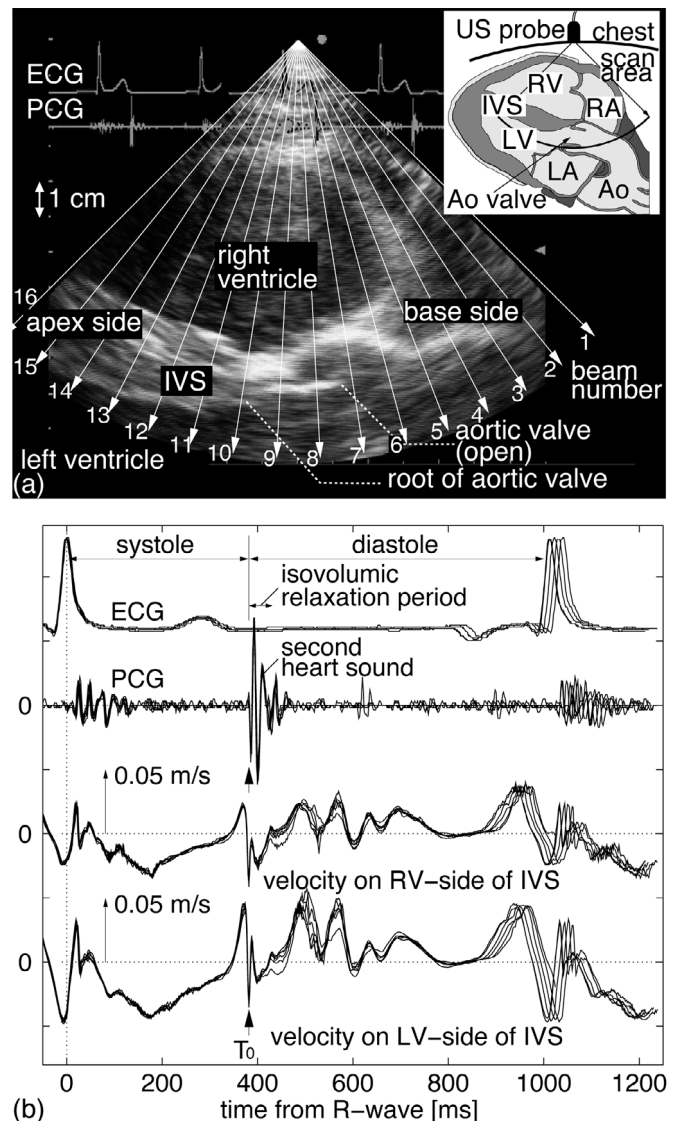

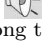





Fig. 1. (a) A cross-sectional image measured by conventional echocardiography in a healthy young male (subject A, 21 years old). The upper-right inset shows the scanning range of the ultrasonic beams in this imaging. The arrows show the directions of the 16 ultrasonic beams used to measure the vibrations at about 160 points in the heart wall. Supplemental animation  shows the conventional B-mode image in the parasternal view obtained by a conventional ultrasonic diagnosis equipment for subject A. The cross-sectional image just before the time of AVC (T_0) from the animation is shown here. (b) *In vivo* measurement results for the healthy man in (a) at two points set along the 13th ultrasonic beam. Each waveform for six consecutive cardiac cycles is overlaid. The time of AVC is denoted by T_0 . Exactly at this time (T_0), a steep dip in the pulsive wave is observed with sufficient reproducibility. The audible vibration signal  was detected for the point preset at the LV side of the IVS along the 13th ultrasonic beam using the method developed for subject A. The audible heart sound  was detected on the chest surface using the microphone for subject A. The audible vibration signal and the heart sound were simultaneously measured. LV, left ventricle; LA, left atrium; RV, right ventricle; RA, right atrium; US probe, ultrasonic probe; IVS, intraventricular septum; Ao, aorta; ECG, electrocardiogram; PCG, phonocardiogram (heart sound).

signals. The phase shift corresponds to the displacement $\Delta x(t)$ during the short-period ΔT and the average velocity $v(t) = \Delta x(t)/\Delta T$ during that period. By accumulating the instantaneous displacement $\Delta x(t)$, the large motion $x(t)$ due to the heartbeat is tracked over one heartbeat; and at the same time, the minute vibration $v(t)$ superimposed on the large motion is obtained as a waveform. For this measurement, the sampling frequency (the time resolution) is increased from the 30 Hz in conventional echocardiography to 450 Hz to avoid aliasing. To realize this, the number of directions in which the ultrasonic beams are transmitted is greatly decreased from 240 to 16 as shown by the arrows in Fig. 1(a).

By applying the above phase tracking method to subject A in Fig. 1(a), Fig. 1(b) shows a typical example of the vibrations on both sides—the right ventricular (RV) side and left ventricular (LV) side—of the IVS. These velocity signals in Fig. 1(b) are audible, similar to the phonocardiogram (PCG) in Fig. 1(a) detected by a microphone on the chest wall. The audible vibration on the LV side along the the 13th ultrasonic beam  and the PCG  is available online. In Fig. 1(b), six consecutive heartbeats are overlaid. Because it is well-known that there are some fluctuations in the duration of diastole even among consecutive cardiac cycles, there are some differences in the six waveforms in the right-hand side of Fig. 1(b). However, during systole and the isovolumic relaxation (IR) period, even the rapid components of the measured vibrations have high reproducibility. As shown by these waves, some discriminative pulsive waves are observed, especially at end systole. Just before the time of AVC (T_0), a slow upward pulse continues for about 30 ms. A steep notch pulse then occurs exactly at T_0 , which coincides with the beginning of the IR period [27].

Using a sparse sector scan in 16 directions, multiple points were preset at 770- μm intervals in the heart wall along each of 16 ultrasonic beams, and the vibrations at about 160 points were simultaneously measured as waveforms with a sampling frequency of 450 Hz by the phased tracking method [24]. Though, in a strict sense, a time lag of $\{(k-1)/16\} \times \Delta T$ is hidden in the sampling time of the vibrations in the direction of the k -th scan line ($k = 1, \dots, 16$), this time lag can be corrected [24]. Fig. 2 shows the simultaneously obtained heart-wall vibrations for all points, but the duration is restricted to the short period from $T_0 - 35$ ms to $T_0 + 35$ ms. The central vertical axis in each wavelet shows the time of AVC (T_0). As shown by the wavelets near the root of the aortic valve, a steep notch pulse occurs at T_0 . The occurrence of this notch is delayed gradually from the root of the aortic valve to the apex by several milliseconds. To the contrary, a steep upward pulse is delayed gradually from the root of the aortic valve to the base.

In the present study, we roughly determined the time of AVC (T_0) by using the heart sound and conventional mo-

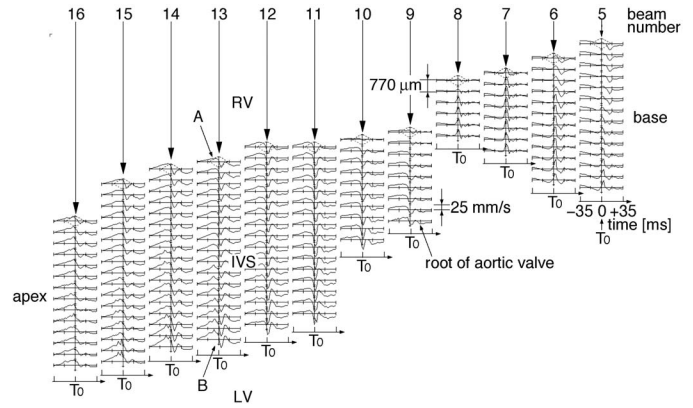



Fig. 2. Spatial distribution of 160 measured wavelets in the IVS at end systole along the 5th to 16th ultrasonic beams in Fig. 1. The subject is the same healthy, young male (subject A) as in Fig. 1, but the measurement was on a different day. These wavelets were simultaneously obtained and shown for the short period between $T_0 - 35$ ms and $T_0 + 35$ ms. The time of AVC (T_0) is determined by the waveform at the LV side along the 9th ultrasonic beam. The two waves A and B correspond to velocity waveforms on the RV side and LV side of the IVS along the 13th ultrasonic beam in Fig. 1(b).

tion picture , but the time resolution was not so high. In [25], the time of AVC (T_0) was determined by the notch on the septal radial myocardial velocity profile in a TDI study, and the correlation between the time of AVC (T_0) determined above and the one measured from the hemodynamic data was confirmed. Thus, we define the exact time of AVC (T_0) as the time of the dip observed in the velocity signal at a point close to the root of the aortic valve. In Fig. 2, this point is at the LV side along the 9th beam.

The displacement of the myocardium due to the steep dip around the time of AVC (T_0) is roughly estimated as $-120 \mu\text{m}$ because the waveform $v(t)$ is approximated by a downward isosceles triangle, the maximum amplitude of the dip is about 30 mm/s, and the duration is about 8 ms. This displacement is far smaller than both the wavelength and the duration of the ultrasound used. Thus, it can be assumed that the preset point stays in the same place in the myocardium during this short period of 70 ms around the time of AVC (T_0).

Because the wavelength of the detected pulsive wave is about 100 mm for a 30-Hz component and is comparable to the size of the whole heart, its propagation phenomenon cannot be clearly visualized by showing the spatial distribution of the instantaneous amplitude of each resultant pulsive wave in Fig. 2. Instead, the phase value varies from 0 to 360 degrees within one wavelength. Therefore, using the method in [24], 2-D spatial distribution of the instantaneous phase values of the measured wave is shown in Fig. 3. For this imaging, the short-time Fourier transform is applied to the pulsive wave at each point in Fig. 2 after the pulsive wave is multiplied by the Hanning window with a short length of 35 ms. The phase value is detected for each frequency component from 10 Hz to 90 Hz, then color coded based on the upper-right circu-

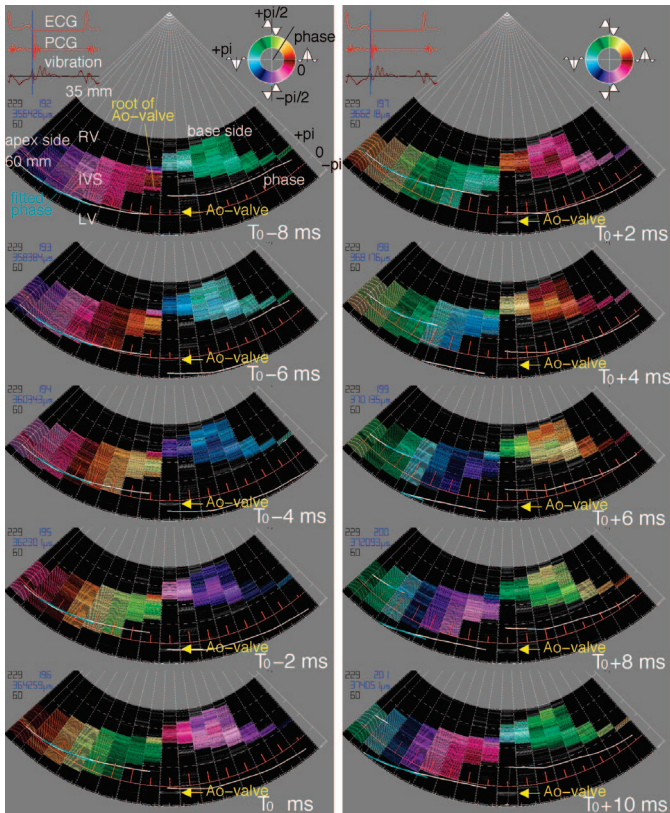


Fig. 3. Spatial distributions of color-coded phase values for 60-Hz component of the wavelets in Fig. 2. The spatial distributions are shown consecutively from $T_0 - 8$ ms to $T_0 + 10$ ms around the time of AVC (T_0). White lines show the instantaneous phase $\theta(x; t)$ used in (1) of the pulsive wave at the LV surface of the IVS, and blue lines show the estimated phase $\hat{\theta}(x; t)$ in (1). These phase values were interpolated between the adjacent ultrasonic beams and are shown here. The supplemental animation [1] shows the distributions of the phase values for 60-Hz component in the parasternal view for subject A. Each figure around the time of AVC (T_0) is shown here.

lar figure in both panels of Fig. 3. In Fig. 3, the phase distributions are shown for a 60-Hz frequency component along the IVS around the time of AVC (T_0). For example, at a time $t = T_0 + 2$ ms in Fig. 3, the phase values vary from cyan (+180 degrees) near the root of the aortic valve, through green (+90 degrees), and to red (0 degree) at the apex. As shown in the upper-right circular figures, the cyan corresponds to the downward pulse that exists exactly at the center position of the multiplied Hanning window. The green corresponds to a 90-degree delay for the downward pulse observed in the analyzed window, and the red corresponds to a 180-degree delay for the same downward pulse. These facts show the possibility that there is a time delay in the spatial distribution and that this time delay gradually increases from 0 ms near the root of the aortic valve to +9 ms ($= +180^\circ / (360^\circ \times f_0)$) near the apex.

Based on the imaging method in [24], Fig. 2 and one of the cross-sectional images in Fig. 3 are obtained. It can be

seen from them that there is a delay in the generated time of the pulsive wave. However, it should be confirmed that the steep pulsive wave does propagate from the base near the root of the aortic valve to the apex. For this purpose, from these consecutively obtained cross-sectional 2-D images in Fig. 3, a motion picture [1] is presented. From the consecutiveness observed in Fig. 3 around the time of AVC (T_0), it can be seen that a few pulsive waves are radiated from the root of the aortic valve and propagate along the IVS. The delay due to the propagation of the pulse from the root to the apex is several milliseconds, which has not been recognized at all by any other clinical technique.

The white lines in Fig. 3 show the instantaneous phase $\theta(x; t)$ of the pulsive wave at the LV surface of the IVS. The phase value is spatially interpolated between each consecutive two points along the adjacent ultrasonic beams. Because there is phase discontinuity between the IVS and the base at the root of the aortic valve, the phase is not connected between the 8th and 9th beams. The instantaneous phase $\theta(x; t)$ spatially varies almost linearly from the root to the apex.

Results of the same measurement applied to four other healthy young male subjects (subjects B-E) can be seen in the motion pictures [1], [2], [3], and [4] of the distribution of the phase values for 60-Hz component. Propagation of the pulsive waves is clearly observed for all these subjects.

Until now in the present study, the shear component with motion along the ultrasonic beam propagating along IVS has been shown in the parasternal view as in Figs. 2, 3, and in motion pictures [1], [2], [3], [4], and [5]. However, by attaching the ultrasonic probe to the apex (apical approach) in in vivo experiments, the longitudinal component propagating along the IVS is shown as follows. Fig. 4 shows a conventional B-mode image of the IVS from the apex just before the time of AVC (T_0) for the same subject A as in Figs. 1, 2, and 3. The conventional motion picture [6] is available online. Because it is necessary to detect a deeper area, the direction in which the ultrasonic beams are transmitted is limited to nine as shown by the arrows in Fig. 4. By applying the same procedure as in Fig. 3, Fig. 5 shows the consecutive spatial distributions of the instantaneous phases for the 60-Hz component of the detected vibrations at all points along the nine beams. Their motion picture [6] reveals that a few pulses also are excited around the time of AVC (T_0) and propagate along the IVS from the root of the aortic valve to the apex.

III. ESTIMATION OF VISCOELASTICITY USING LAMB WAVE AND VOIGT MODELS

Based on these results, in this section, the principle of determination of the phase velocity and modeling of the pulsive wave are proposed to estimate the myocardial viscoelasticity.

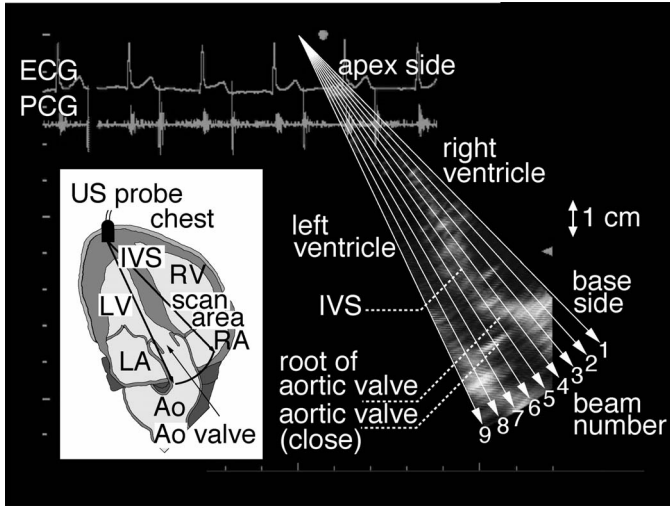



Fig. 4. Cross-sectional image in the apical view exactly at the time of AVC ($t = T_0$) measured by a conventional ultrasonic diagnosis system for the same subject A as in Figs. 1, 2, and 3. Nine ultrasonic beams were used to measure the vibrations at points preset in the IVS for Fig. 5. The blue lines show the directions of the nine ultrasonic beams. The supplemental animation  shows the conventional B-mode image in the apical approach obtained by a conventional ultrasonic diagnosis equipment for subject A. This figure shows the cross-sectional image just at the time of AVC (T_0).

To determine the instantaneous phase velocity of the pulsive wave, if the straight line with a constant gradient k [rad/m] is spatially fit to the instantaneous spatial distribution of the measured phase in the region on the left-hand side in each cross-sectional image in Fig. 3, the instantaneous phase velocity for the frequency component f_0 is determined by $2\pi f_0/k$. However, because there is initially some spatial distribution of the phase that is independent of the propagation, the wavelength and thus the wave number k do not correspond to the actual phase velocity.

Therefore, in this study, based on the definition of the phase velocity, the distance Δx between two consecutively obtained phase distributions is determined. For this, the phase distribution $\theta(x; t)$ at a time t is compared with the shifted phase distribution $\theta(x + \Delta x; t - \Delta T)$ obtained at a time $t - \Delta T$. In actual calculation, a complex exponential function is introduced so that no special unwrapping procedure is necessary for the phase jump between $-\pi$ and $+\pi$. The root $\gamma(\Delta x; \omega)$ of the averaged squared difference between the two exponential functions of $\theta(x; t)$ and $\theta(x + \Delta x; t - \Delta T)$ for the angular frequency ω is defined by:

$$\gamma(\Delta x; \omega) = \sqrt{\frac{\sum_x |\exp\{j\theta(x; t)\} - \exp\{j\theta(x + \Delta x; t - \Delta T)\}|^2}{\sum_x |\exp\{j\theta(x; t)\}|^2}}. \quad (1)$$

The optimum distance $\widehat{\Delta x}$ is determined so that the root $\gamma(\Delta x; \omega)$ is minimized. The phase velocity c_{phase}

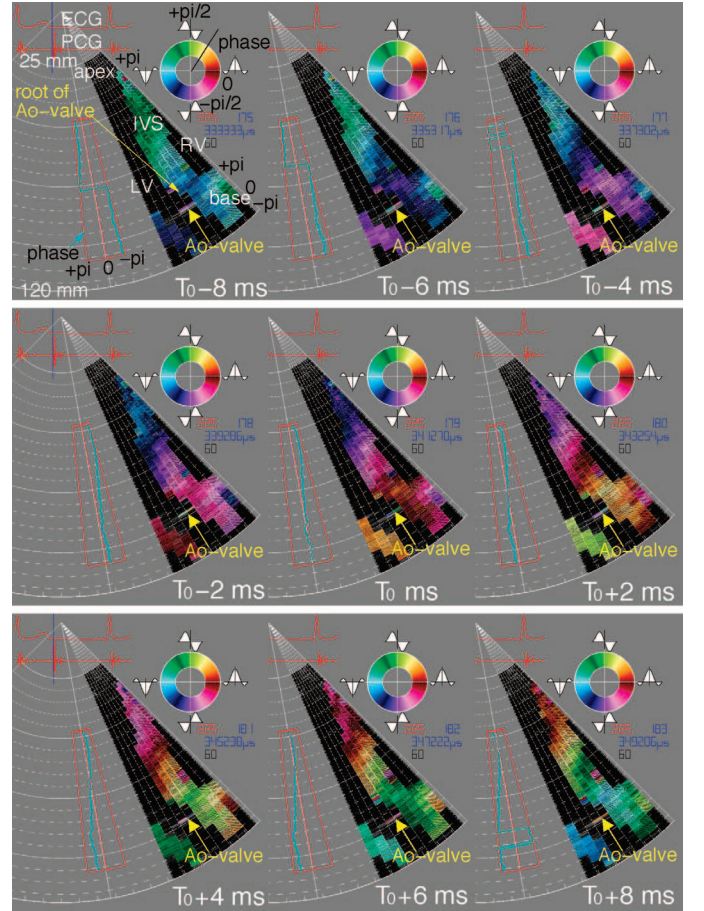




Fig. 5. For the data in Fig. 4, the spatial distributions in the apical view of color-coded phase values for the 60-Hz component of the measured wavelets consecutively from $T_0 - 8$ ms to $T_0 + 8$ ms around the time of AVC (T_0). The blue line in the left-hand side of each figure shows the instantaneous phase $\theta(x; t)$ along the 4th ultrasonic beam. The phase jump is not unwrapped. The supplemental animation  shows the distribution of the phase values for 60-Hz component in the apical view for subject A. Each figure around the time of AVC (T_0) is shown here.

[m/s] then is obtained for each angular frequency ω by $c_{\text{phase}}(\omega) = \widehat{\Delta x}/\Delta T$, where $\Delta T = 1.96$ ms for the experiment.

Regarding the phenomenon of the wave propagation along the viscoelastic plate with thickness $2h$, it is well-known that there are three kinds of plate wave [28]–[31], that is: the shear horizontal (SH)-wave, the Lamb wave with symmetric mode (shear vertical (SV) wave with extensional vibration), and the Lamb wave with asymmetric mode (SV-wave with flexural vibration as illustrated in Fig. 6), in which symmetric and asymmetric refer to the central plane ($y = 0$ in Fig. 6) of the plate. In the parasternal longitudinal-axis view of Fig. 3, the direction ($-y$) of each ultrasonic beam is almost perpendicular to the IVS, and the detected motion is along each beam (y -direction in Fig. 6). As shown in Fig. 3 and the motion picture 

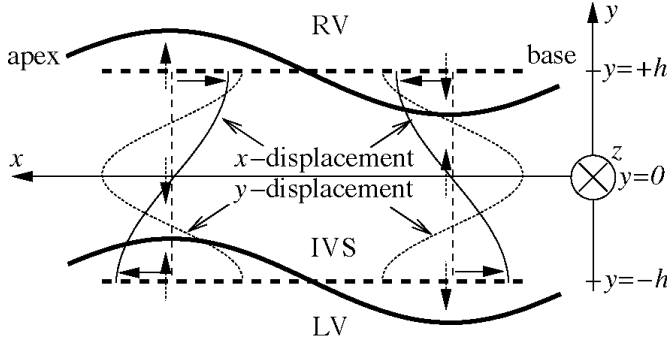


Fig. 6. Lamb wave with asymmetric mode of plate waves in the viscoelastic plate with thickness $2h$. The SV-wave component (y -displacement) and longitudinal component (x -displacement) are coupled; the Lamb wave then propagates along the x -direction. Although a slightly higher order mode is illustrated, the lowest mode is probably dominant in actual vibration in the IVS.

the pulsive wave propagates along the IVS (x -direction). As shown in the spatial distribution of Fig. 2, the vibrations at the RV side and those at the LV side are almost parallel (asymmetric). The wavelength λ is about 100 mm for the 30-Hz component and 40–65 mm for the 90-Hz component. The thickness $2h$ of the IVS is about 10 mm in healthy adults. Thus, the thickness is sufficiently thin. Moreover, Fig. 5 and the motion picture [14] show that the longitudinal component with x -displacement also propagates along the IVS (x -direction). By comparing Fig. 3 and the motion picture [14] with Fig. 5 and the motion picture [14], the propagation speed of the shear component is seen to be close to that of the longitudinal component. Thus, there is a likelihood of coupling between the SV component and the longitudinal component. Given these facts, the detected vibration signal can be modeled by a Lamb wave with asymmetric mode in Fig. 6. Though the wavelength of 100 mm at 10 Hz corresponds to the size of the whole heart, the duration of the notch pulse is very short (10 ms), corresponding to about 1 cm in length. Thus, the traveling wave does not overlap the reflected wave in this measurement.

For the IVS, the blood in RV and LV should be considered. Thus, the model of the Lamb wave of Fig. 6, propagating along the viscoelastic plate (IVS) immersed in blood, is used in the present study. Let us define the wave number of the Lamb wave by k_L . By referring to equation 4.24 in [31], the function—termed $f(k_L, k_p, k_s)$, which should be zero—is given by:

$$\begin{aligned} f(k_L, k_p, k_s) = & 4k_L^2 \eta \beta \cosh(\eta h) \sinh(\beta h) \\ & - (2k_L^2 - k_s^2)^2 \sinh(\eta h) \cosh(\beta h) \\ & - \frac{\rho_b \eta k_s^4}{\rho_m \eta_b} \cosh(\eta h) \cosh(\beta h) = 0, \end{aligned} \quad (2)$$

where k_p and k_s are the wave numbers of the primary (longitudinal) wave and the secondary (shear) wave, respectively, in the myocardium. Using k_p , k_s , and the wave number k_b in blood, η , β , and η_b are defined by

$\eta = \sqrt{k_L^2 - k_p^2}$ [rad/m], $\beta = \sqrt{k_L^2 - k_s^2}$ [rad/m], and $\eta_b = \sqrt{k_L^2 - k_b^2}$ [rad/m]. ρ_m and ρ_b are the myocardium density and the blood density, respectively, and ρ_m can be approximated by $\rho_b = 1.1 \times 10^3$ kg/m³. The thickness $2h$ of the IVS is determined from the conventional B-mode image.

$$\mu \ll \lambda$$

By introducing a single Voigt dash-pot model in the frequency range up to 90 Hz, the Lamé elastic constants λ and μ become complex values as $\lambda = \lambda_1 + j\omega\lambda_2$ [Pa] and $\mu = \mu_1 + j\omega\mu_2$ [Pa], respectively [32]. Because λ is about 10^3 times larger than μ for soft tissue due to noncompressibility [32], k_p is approximated by $k_p = \omega\sqrt{\rho_m/(\lambda + 2\mu)} \approx \omega\sqrt{\rho_m/\lambda} = k_b$. Because the wave number k_L of the Lamb wave is close to k_s , k_L^2 is about 10^3 times larger than k_p^2 . Thus, $\eta = \sqrt{k_L^2 - k_p^2} \approx k_L$ and $\eta_b = \sqrt{k_L^2 - k_b^2} \approx k_L$. Therefore, $f(k_L, k_p, k_s)$ of (2) is approximated by:

$$\begin{aligned} f'(c_L, \mu, \omega) = & 4k_L^2 \beta \cosh(k_L h) \sinh(\beta h) \\ & - (2k_L^2 - k_s^2)^2 \sinh(k_L h) \cosh(\beta h) \\ & - k_s^4 \cosh(k_L h) \cosh(\beta h) = 0, \end{aligned} \quad (3)$$

where $k_L = \omega/c_L(\mu, \omega)$ [rad/m] and $k_s = \omega\sqrt{\rho_m/\mu}$ [rad/m]. Thus, $f'(c_L, \mu, \omega)$ depends on both the phase velocity $c_L(\mu, \omega)$ of the Lamb wave and the Lamé elastic constant $\mu = \mu_1 + j\omega\mu_2$.

Based on the model described above, the theoretical value of the phase velocity $c_L(\mu, \omega)$ of the Lamb wave is determined to be close to the measured phase velocity $c_{\text{phase}}(\omega)$, where $c_L(\mu, \omega)$ depends on $\mu = \mu_1 + j\omega\mu_2$. For the nonlinear optimization, we follow the procedure described below.

Assuming one combination of values μ_1 and μ_2 , μ is given for an angular frequency ω . For the value of μ , by setting one value of the phase velocity $c_L(\mu, \omega)$, the wave number $k_L = \omega/c_L$ and all other parameters included in $f'(c_L, \mu, \omega)$ of (3) can be obtained. The phase velocity $c_L(\mu, \omega)$ then is determined for the assumed value μ so that $f'(c_L, \mu, \omega)$ becomes zero. Actually, $\hat{c}_L(\mu, \omega)$ is chosen so that the absolute value $\|f'(\hat{c}_L, \mu, \omega)\|$ is closest to zero. By varying the angular frequency ω , the values $\{\hat{c}_L(\mu, \omega)\}$ of the phase velocity are all determined for the assumed value μ . Thus, the root of the normalized mean squared difference, $\alpha(\mu_1, \mu_2)$, between these theoretical phase velocities $\{\hat{c}_L(\mu, \omega)\}$ and the measured ones $\{c_{\text{phase}}(\omega)\}$ is defined as:

$$\alpha(\mu_1, \mu_2) = \sqrt{\frac{\sum_{\omega} w(\omega)^2 |c_{\text{phase}}(\omega) - \hat{c}_L(\mu, \omega)|^2}{\sum_{\omega} w(\omega)^2}} \quad [\text{m/s}], \quad (4)$$

where $w(\omega)$ is the weight for each measurement of $c_{\text{phase}}(\omega)$ and corresponds to its reliability. In this study, the inverse of the minimum of the squared difference $\gamma(\Delta x; \omega)$ of (1) between the consecutive phase distributions is used as $w(\omega)$. By scanning the combination of the complex value μ , the optimum Lamé constant $\hat{\mu} = \hat{\mu}_1 + j\omega\hat{\mu}_2$ is determined so that $\alpha(\mu_1, \mu_2)$ is minimized:

$$\alpha_{\min}(\hat{\mu}_1, \hat{\mu}_2) = \min_{\mu_1, \mu_2} \alpha(\mu_1, \mu_2) \text{ [m/s]}. \quad (5)$$

By this procedure, for each time t , from the measured dispersion, the optimum Lamé constant $\hat{\mu}$ (shear elastic constant $\hat{\mu}_1$ and shear viscosity constant $\hat{\mu}_2$) is determined using the model of the Lamb wave that propagates along the thin viscoelastic plate (IVS) immersed in blood.

IV. IN VIVO EXPERIMENTAL RESULTS FOR HEALTHY SUBJECTS

By analyzing the spatial distribution of the phase of each wavelet in Fig. 2 for each time from $T_0 - 8$ ms to $T_0 + 10$ ms and for each frequency component from 10 Hz to 90 Hz, the instantaneous phase velocity $c_{\text{phase}}(\omega)$ was obtained as in Fig. 7(b). There is dispersion among the instantaneous phase velocities $\{c_{\text{phase}}(\omega)\}$, and they rapidly decrease for all frequency components in this short period around the time of AVC (T_0). Exactly at the time of AVC (T_0), the instantaneous phase velocities $\{c_{\text{phase}}(\omega)\}$ of the 27-, 60-, and 87-Hz components are 2.0, 4.0, and 4.5 m/s, respectively. As described in Section V, the order of magnitude of these velocity values is similar to those measured in in vitro experiments in the literature.

Fig. 7(c) shows the minimum $\gamma(\hat{\Delta x}; \omega)$ of the root of the averaged squared difference of (1) for the frequency of $f = \omega/2\pi$ hertz. For higher frequencies, the errors become larger. However, for less than 70 Hz, the velocity estimate $c_{\text{phase}}(\omega)$ is fairly reliable. These errors are used as the inverse of the weight $w(\omega)$ in (4).

The phase velocity of the longitudinal component propagating from the root of the aortic valve to the apex was determined as follows. The blue line in each panel of Fig. 5 shows the spatial distribution of the phase $\theta(x; t)$ for the 60-Hz component. In the depth range from 60 mm to 90 mm, the phase velocity $c_{\text{phase}}(f)$ was determined based on the procedure in Section III-A. At a time $T_0 - 10$ ms, $c_{\text{phase}}(f)$ is 5.5 m/s for the 60-Hz component. As time increases, $c_{\text{phase}}(f)$ gradually decreases, and at a time $T_0 + 10$ ms, $c_{\text{phase}}(f)$ is 4.0 m/s. These velocity values are close to those of the shear component obtained in Fig. 7(b).

For subject A, the estimated elasticity is about 24–30 kPa and does not change around the time of AVC. In the experiments, the viscosity can be determined more

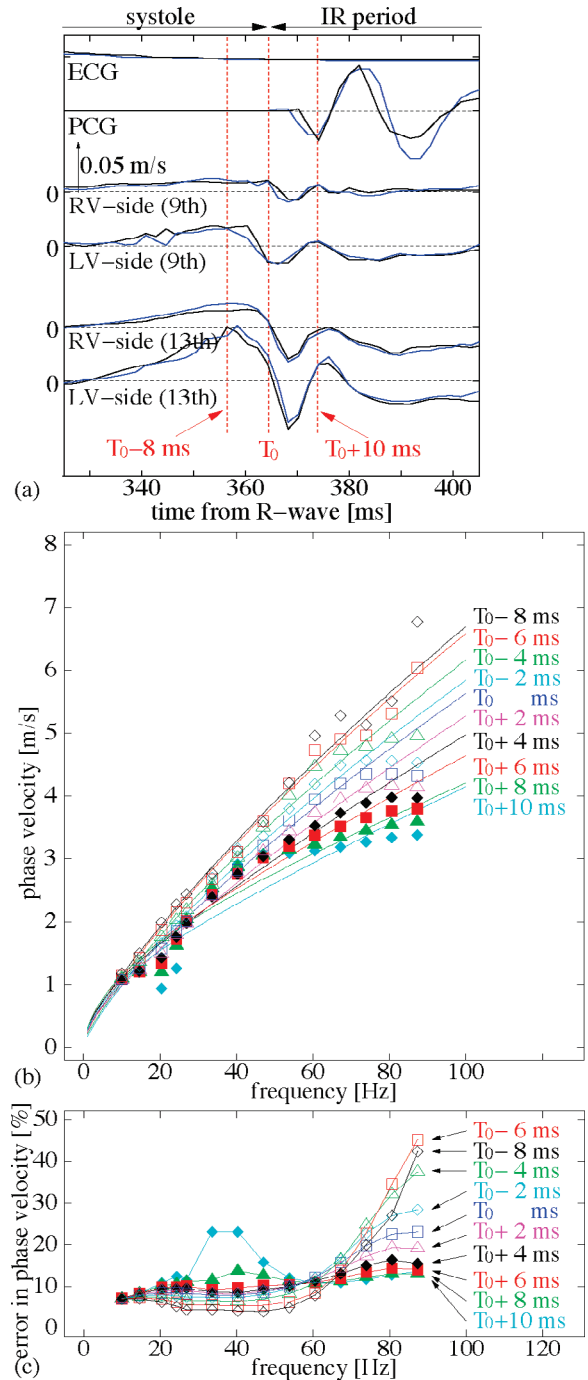


Fig. 7. (a) The analyzed period from $T_0 - 8$ ms to $T_0 + 10$ ms in Fig. 3 is shown by using the waveforms of electrocardiogram (ECG), those of PCG, velocity signals at the RV side along the 9th ultrasonic beam, velocity signals at the LV side along the 9th ultrasonic beam, velocity signals at the RV side along the 13th ultrasonic beam, and velocity signals at the LV side along the 13th ultrasonic beam. Each waveform contains the signals for two consecutive cardiac cycles. (b) Measured instantaneous phase velocity values $\{c_{\text{phase}}\}$ and fitted theoretical curves $\hat{c}_L(\hat{\mu}, f)$ using the optimization procedure in Section III-D for the frequency components from 10 Hz to 90 Hz during the period from $T_0 - 8$ ms to $T_0 + 10$ ms in (a). (c) For each time from $T_0 - 8$ ms to $T_0 + 10$ ms, the achieved minimum $\gamma(\hat{\Delta x}; \omega)$ of the root of the averaged squared difference between the phase components of (1), where $f = \omega/2\pi$ Hz.

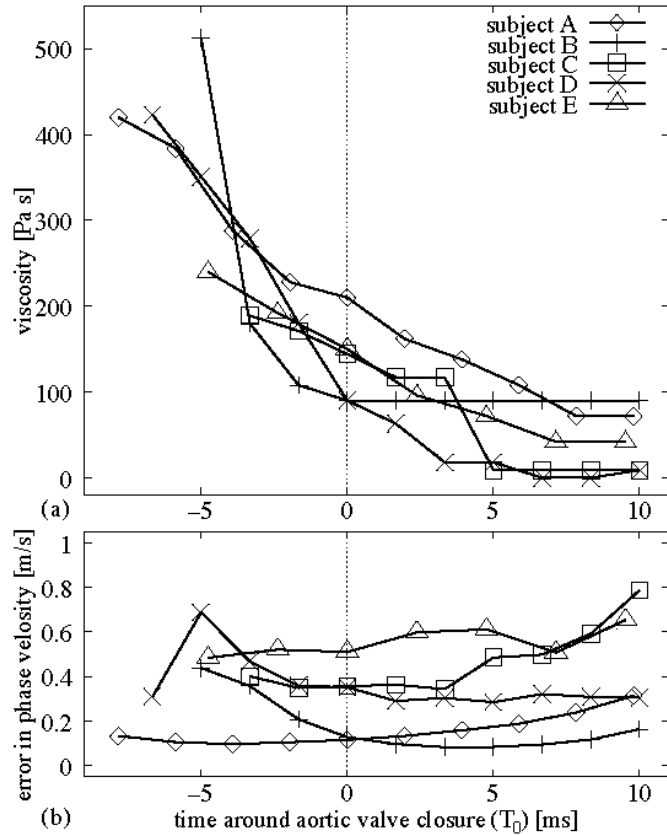



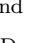


Fig. 8. (a) Transient of the viscosity parameters $\{\mu_2\}$ measured during the period from $T_0 - 8$ ms to $T_0 + 10$ ms in Fig. 7 for five healthy young male subjects, including subject A. Supplemental animation of the distribution of the phase values for 60-Hz component is available, showing the distribution of the phase values for 60-Hz component in the parasternal view for subjects B , C , D , and E . Subject B, 25 years old; subject C, 21 years old; subject D, 25 years old; and subject E, 23 years old. (b) The minimum value $\alpha_{\min}(\hat{\mu}_1, \hat{\mu}_2)$ [m/s] of the normalized mean squared difference of (5) for each subject.

precisely than the elasticity. In Section V, the preciseness in the estimation of the elasticity and the viscosity is discussed. The transient of the viscosity $\{\mu_2\}$ determined for each time from $T_0 - 8$ ms to $T_0 + 10$ ms in Fig. 7 for subject A is shown in Fig. 8(a). Around the beginning of the IR period, the instantaneous viscosity of the myocardium rapidly decreases from about 400 Pa·s to 70 Pa·s. As described in Section V, this would be due to the rapid decrease in the LV inner pressure from about 120 mmHg to several millimeters of mercury, which is caused by relaxation of the myocardium.

For the other four subjects, B–E, the same measurement and analysis were applied, and similar transient characteristics of the viscosity were obtained as shown in Fig. 8(a).

Fig. 8(b) shows the minimum value $\alpha_{\min}(\hat{\mu}_1, \hat{\mu}_2)$ of the mean squared difference of (5) between the measured phase velocities $\{c_{\text{phase}}(\omega)\}$ and the theoretical ones $\{\hat{c}_L(\mu, \omega)\}$ for each analysis. The errors are at most 0.3–0.8 m/s in the analysis. These errors correspond to about 10–20% of the phase velocity at the center frequency (50 Hz).

Using the estimated Lamé constant $\hat{\mu}$, the phase velocity $\hat{c}_L(\hat{\mu}, f)$ is obtained in the procedures in Section III-D. The results are shown by the solid lines in Fig. 7(b) for each time t . The estimates $\{\hat{c}_L(\hat{\mu}, f)\}$ well fit the measured dispersion characteristics $c_{\text{phase}}(f)$ in Fig. 7(b).

V. DISCUSSION

As shown in Section IV-A, the phase velocity measured in the present study ranges from 1 to 7 m/s for the relaxation phase. As shown in Table I, the order of magnitude of the phase velocity values is similar to those measured recently using low-frequency, shear-wave vibrations reported in the literature for human quadriceps muscle [2], for human bicep muscle [5], for pig leg/shoulder muscles [1], and for beef muscle [4]. It is known that the propagation speed of the electrically excited waves along the cardiac muscle and the Purkinje fiber in the myocardium is about 0.3 m/s [8], [9] and 2–3 m/s [10], respectively. However, the electrical excitation mainly occurs around the beginning of the ejection period. Therefore, the pulsive wave propagation found around the AVC in the present study is a mechanical phenomenon.

For the IR period, in which the myocardial viscoelasticity is estimated, the myocardium can be characterized as being passive. The clinical effect of such viscous properties before the onset of filling on myocardium relaxation was investigated in [33]. Application of the present method to the beginning of systole, in which the mitral valve closes and the first heart sound is radiated, could possibly contribute to the determination of the active properties of the myocardium as modeled in [34], [35].

The elastic values and viscosity values obtained in the present study are compared with those reported for the myocardium and soft tissues in the literature as follows. The methods used can be divided into the following two categories with regard to the frequency (see Table II). Except for those of the present study, all data were measured in *in vitro* experiments.

In [36], by the ultrasonic measurement of transverse-mode acoustic impedance at 2–14 MHz, the shear stiffness μ_1 and viscosity μ_2 were obtained as 1 MPa and 0.004–0.03 Pa·s for canine soft tissue. In [37], using a similar method, μ_1 and μ_2 were 124 kPa and 0.0159 Pa·s, respectively, for the cardiac muscle. In [38], using a 3-MHz transverse mode propagated perpendicular to the fiber axis of a formalin-fixed normal human myocardium, the stiffness (C_{66}) and viscosity, calculated from the velocity and attenuation, were 8.45 MPa and 0.404 Pa·s, respectively.

On the contrary, with mechanical measurement using audio or lower frequency components, using a surface wave [39], the elastic component (C_{66}) and viscosity (μ_2) were measured as 5 kPa and 1.6 Pa·s, respectively, at 2 kHz for bovine myocardium [40]. In [32], for the low frequency of 500–5,000 Hz, the shear parameters were measured as $\mu = 2.5 \text{ kPa} + j15 \text{ Pa}\cdot\text{s}$ for human muscle tissue. In [41], for the canine left ventricle, using pressure perturbations, μ_1

TABLE I

TYPICAL VALUES OF SPEED OF THE SHEAR WAVE MEASURED FOR SOFT TISSUES IN THE LITERATURE AND PRESENT STUDY.

Frequency used	Speed of sound	Measured region	Reference
20 Hz	1–2 m/s	Human myocardium (during IR, in vivo)	Present study (Fig. 7)
30–120 Hz	4–5.4 m/s	Human quadriceps (in vivo)	[2]
50 Hz	3–4 m/s	Human myocardium (during IR, in vivo)	Present study (Fig. 7)
50 Hz	About 2 m/s	Human bicep (no load)	[5]
90 Hz	3–7 m/s	Human myocardium (during IR, in vivo)	Present study (Fig. 7)
100–225 Hz	5–6.5 m/s	Pig leg and shoulder muscle	[1]
About 150 Hz	5.3 m/s	Beef muscle (2-ms pulsed excitation)	[4]

TABLE II

TYPICAL VALUES OF THE ELASTICITY μ_1 AND VISCOSITY μ_2 MEASURED FOR SOFT TISSUES IN THE LITERATURE AND PRESENT STUDY.¹

Frequency used	Elasticity μ_1	Viscosity μ_2	Measured region	Reference
About 2 Hz	290–1,460 kPa	2,800–19,000 Pa·s	Canine descending thoracic aorta to femoral artery	[43]
10 Hz	1,000–7,000 kPa	5,000–30,000 Pa·s	Human carotid artery to human femoral artery	[42]
20 Hz	7.5 kPa	75 Pa·s	Pig kidney	[44]
22 Hz	30–400 kPa	200–1,400 Pa·s	Canine left ventricle	[41]
10–90 Hz	30 kPa	70–400 Pa·s	Human myocardium (in vivo)	Present study
50 Hz	30–400 kPa	30–200 Pa·s	Cow muscle	[45]
50 Hz	30 kPa	30 Pa·s	Cow muscle (freshest)	[45]
150 Hz	21 kPa	23 Pa·s	Beef muscle	[4]
500–5,000 Hz	2.5 kPa	15 Pa·s	Human muscle tissue	[32]
2,000 Hz	5 kPa	1.6 Pa·s	Bovine myocardium	[40]
3 MHz	8,450 kPa	0.4 Pa·s	Formalin fixed human myocardium	[38]
2–14 MHz	124 kPa	0.02 Pa·s	Cardiac muscle	[37]
2–14 MHz	1,000 kPa	0.004–0.03 Pa·s	Canine soft tissue	[36]

¹Except for the present study, all data were measured in in vitro experiments.

and μ_2 were determined as 30–400 kPa and 200–1,400 Pa·s, respectively, for 22 Hz. In [42], the artery was subjected to pressure oscillations, and μ_1 and μ_2 were measured from the human carotid artery to the femoral artery. For 10 Hz, μ_1 and μ_2 were 1–7 MPa and 5–30 kPa·s, respectively. Similar experiments were conducted in [43]. In [44], using a standard strain-controlled rheometer, the shear elasticity and viscosity of fresh pig kidney were 1–7.5 kPa and 20–75 Pa·s, respectively, for 0.01 to 20 Hz with a strain of 0.2%. In [45], by applying an electromagnetic transducer to muscle tissue taken from freshly killed cows in a frequency range from 25–2,500 Hz, in which the shear stress was applied parallel to the muscle fibers, $\mu_1 = 30$ –400 kPa and $\mu_2 = 30$ –200 Pa·s for 50 Hz. Especially in the freshest specimen, the values were lower at $\mu_1 = 30$ kPa and $\mu_2 = 30$ Pa·s for 50 Hz. The elasticity slightly increased with increased frequency, but the viscosity remarkably decreased with the increase in frequency. In [45], moreover, it was experimentally found that both μ_1 and μ_2 increase with time after slaughtering. That paper [45] discussed that this dependency on the elapsed time is related to the loss of water from the fresh tissue.

Roughly speaking, the elasticity is large for very low frequency less than 10 Hz and for frequency higher than 1 MHz. In [44], the experimental results for pig kidney

showed that the elasticity increases with frequency in the frequency range from 0.01 Hz to 20 Hz. The viscosity data are well fitted to $\mu_2 = 626.7 \times f^{-0.722}$ [Pa·s], which shows that the viscosity decreases with the increase in frequency f . Especially at megahertz frequencies (in the first category above), the viscosity values in the literature are much lower than those reported at audio frequencies (in the second category). By considering the frequency dependency and the freshness of the specimens in Table II, the elasticity and viscosity measured in the present study are close to those measured for the same frequency range in the literature.

In [46], the anisotropy of the speed of sound and the elastic properties have been measured. In the actual heart wall, along the radial axis (the thickness direction) of the LV, the myocardial fiber orientation changes gradually. For patients with hypertrophic cardiomyopathy, parallel alignment of muscle cells becomes irregular (myocardial disarray). However, in the present study, such anisotropy and change in fibrous orientation are not considered at all.

When the preciseness of elasticity and viscosity is compared, it is apparent that the elasticity is not precisely estimated. The reason is due to the fitting of the theoretically derived phase values $\{c_L(\mu, f)\}$ to the measured ones $\{c_{\text{phase}}(f)\}$. Because the Voigt model $\mu = \mu_1 + j\omega\mu_2$ is

used, the gradient of the dispersion characteristics in Fig. 7 mainly depend on the viscosity μ_2 , and there is large dispersion in the frequency range from 10 to 90 Hz in these in vivo experiments. Thus, the viscosity is relatively precisely estimated. However, the elasticity μ_1 corresponds to the bias component (the velocity of the frequency components close to 0 Hz) of the dispersion characteristics. Because the detected notch pulse is nonstationary and the short-time Fourier transform is applied to the pulse, it is difficult to detect its very low frequency components and the propagation. Thus, the viscosity can be precisely determined, but the elasticity cannot.

In Section III-B, the model in which the viscoelastic plate is immersed in blood is used. The blood density ρ_b , the myocardium density ρ_m , the longitudinal velocity c_b in blood, and the longitudinal velocity c_m in the myocardium can be approximated as being almost constant for blood pressure ranging from 0–120 mmHg. It is known that the viscosity in muscle highly depends on the velocity of the stretch [47] or the instantaneous muscle length [34]. However, in the short period analyzed in the present study, the change in length is negligible. According to [2] and [5], the shear wave velocity and shear elasticity of the human muscle increase as a load is applied in in vivo experiments. As in [48] and [49], the viscosity also depends on the pressure. Thus, there is a close relationship between the transient of the viscosity obtained in Fig. 8(a) and the change in inner pressure of the LV. Thus, the blood pressures in RV and LV and their transient should be further introduced into the boundary conditions for the wave equations.

The estimation process of the viscoelasticity in this study should be validated using an elastic spherical shell as a heart phantom; this is currently being conducted. By such phantom experiments, it also should be confirmed whether the transient characteristics in viscosity correspond to the change in inner pressure.

In [50], experimental results on soft tissue have been discussed in the framework of the linear theory of viscoelasticity relating stress and strain on the basis of the Voigt, Maxwell, and Kelvin models. The main objective of these models is to identify the parameters that are directly related to the mechanical behavior of the constituents of the tissue to produce a simple description of the gross mechanical behavior of the tissue. Such behavior is influenced by collagen and its interactions with other components of the tissue [44], by water content [45], and by time after death [51]. Not only the myocardial elasticity but also the viscosity depend on the interaction between the giant muscle protein titin and actin filaments in the sarcomere during both diastolic stretch and systolic shortening [52]. However, the mechanical response of many soft tissues to mechanical loading is not well described by current models in [44]. Thus, the physiological origin of the myocardial viscoelasticity should be further investigated. At the same time, more accurate modeling, such as the Maxwell or Kelvin models and their combinations, should be undertaken, whereas the Voigt model was used in the present study. Many researchers have measured the relax-

ation time in the step response of the soft tissue [34], [53], in which the relaxation time can be compared with the viscosity using appropriate modeling.

VI. CONCLUSIONS

We measured rapid and minute vibrations simultaneously at multiple points in the IVS. We found that the pulsive wave is spontaneously actuated due to the AVC at the beginning of the IR period. Clear propagation of the pulsive wave along the IVS was recognized for the first time. From the dispersion of the phase velocities, the myocardial viscoelasticity was determined noninvasively for the first time. This method offers potential for in vivo imaging of the spatial distribution of the passive mechanical properties of the myocardium and its rapid change during the IR period, which would enable direct assessment of diastolic properties based on myocardial relaxation in heart failure [54], [55], which cannot be obtained by conventional echocardiography, CT, or MRI.

ACKNOWLEDGMENTS

The author is grateful to the reviewers of the present paper for helpful and valuable advice. The author also is grateful to Prof. Emeritus Motonao Tanaka of Tohoku University, Prof. Floyd Dunn of the Bioacoustics Research Laboratory of the University of Illinois, and Dr. Jens E. Wilhjelm of the Technical University of Denmark for useful discussions. The author also acknowledges the experimental contributions of Dr. Hideyuki Hasegawa in our laboratory.

REFERENCES

- [1] Y. Yamakoshi, J. Sato, and T. Sato, "Ultrasonic imaging of internal vibration of soft tissue under forced vibration," *IEEE Trans. Ultrason., Ferroelect., Freq. Contr.*, vol. 37, no. 2, pp. 45–53, 1990.
- [2] S. F. Levinson, M. Shinagawa, and T. Sato, "Sonoelastic determination of human skeletal muscle elasticity," *J. Biomechan.*, vol. 28, no. 10, pp. 1145–1153, 1995.
- [3] S. Catheline, J.-L. Thomas, F. Wu, and M. A. Fink, "Diffraction field of a low frequency vibrator in soft tissues using transient elastography," *IEEE Trans. Ultrason., Ferroelect., Freq. Contr.*, vol. 46, no. 4, pp. 1013–1019, 1999.
- [4] S. Catheline, F. Wu, and M. Fink, "A solution to diffraction biases in sonoelasticity: The acoustic impulse technique," *J. Acoust. Soc. Amer.*, vol. 105, no. 5, pp. 2941–2950, 1999.
- [5] L. Sandrin, M. Tanter, J.-L. Gennisson, S. Catheline, and M. Fink, "Shear elasticity probe for soft tissues with 1-D transient elastography," *IEEE Trans. Ultrason., Ferroelect., Freq. Contr.*, vol. 49, no. 4, pp. 436–446, 2002.
- [6] V. Dutt, R. R. Kinnick, and J. F. Greenleaf, "Acoustic shear wave displacement using ultrasound," in *Proc. IEEE Ultrason. Symp.*, 1996, pp. 1185–1188.
- [7] S. Chen, M. Fatemi, and J. F. Greenleaf, "Complex stiffness quantification using ultrasound stimulated vibrometry," in *Proc. IEEE Ultrason. Symp.*, 2003, pp. 941–944.
- [8] O. Anosov, S. Berdyshev, I. Khassanov, M. Schaldach, and B. Hensel, "Wave propagation in the atrial myocardium: Dispersion

- properties in the normal state and before fibrillation," *IEEE Trans. Biomed. Eng.*, vol. 49, no. 12, pp. 1642–1645, 2002.
- [9] S. P. Thomas, J. P. Kucera, L. Bircher-Lehmann, Y. Rudy, J. E. Saffitz, and A. G. Kléber, "Impulse propagation in synthetic strands of neonatal cardiac myocytes with genetically reduced levels of connexin43," *Circ. Res.*, vol. 92, pp. 1209–1216, 2003.
- [10] N. Sperelakis, "Origin of the cardiac resting potential," in *Handbook of Physiology. The Cardiovascular System*. R. M. Berne, N. Sperelakis, and S. R. Geiger, Eds. Bethesda, MD: American Physiological Society, 1979, p. 190.
- [11] L. T. Mahoney, W. Smith, M. P. Noel, M. Florentine, D. J. Skorton, and S. M. Collins, "Measurement of right ventricular volume using cine computed tomography," *Invest. Radiol.*, vol. 22, no. 6, pp. 451–455, 1987.
- [12] E. A. Zerhouni, D. M. Parish, W. J. Rogers, A. Yang, and E. P. Shapiro, "Human heart: Tagging with MR imaging—A method for noninvasive assessment of myocardial motion," *Radiology*, vol. 169, pp. 59–63, 1988.
- [13] L. Axel, R. C. Goncalves, and D. Bloomgarden, "Regional heart wall motion: Two-dimensional analysis and functional imaging with MR imaging," *Radiology*, vol. 183, no. 3, pp. 745–750, 1992.
- [14] A. D. Fleming, X. Xia, W. N. McDicken, G. R. Sutherland, and L. Fenn, "Myocardial velocity gradients detected by Doppler imaging," *Br. J. Radiol.*, vol. 67, no. 799, pp. 679–688, 1994.
- [15] R. S. Adler, J. M. Rubin, P. H. Bland, and P. L. Carson, "Quantitative tissue motion analysis of digitized M-mode images: Gestational differences in fetal lung," *Ultrasound Med. Biol.*, vol. 16, no. 6, pp. 561–569, 1990.
- [16] G. R. Sutherland, M. J. Stewart, K. W. E. Groundstroem, C. M. Moran, A. Fleming, F. J. Guell-Peris, R. A. Riemersma, L. N. Fenn, K. A. A. Fox, and W. N. McDicken, "Color Doppler myocardial imaging: A new technique for the assessment of myocardial function," *J. Amer. Soc. Echocardiogr.*, vol. 7, pp. 441–458, 1994.
- [17] A. Heimdal, A. Støylen, H. Torp, and T. Skjærpe, "Real-time strain rate imaging of the left ventricle by ultrasound," *J. Amer. Soc. Echocardiogr.*, vol. 11, pp. 1013–1019, 1998.
- [18] K. Miyatake, M. Yamagushi, N. Tanaka, M. Uematsu, N. Yamazaki, Y. Mine, A. Sano, and M. Hirama, "New method for evaluating left ventricular wall motion by color-coded tissue Doppler imaging: *in vitro* and *in vivo* studies," *J. Amer. Coll. Cardiol.*, vol. 25, no. 3, pp. 717–724, 1995.
- [19] P. Palka, A. Lange, A. D. Fleming, G. R. Sutherland, L. N. Fenn, and W. N. McDicken, "Doppler tissue imaging: Myocardial wall motion velocities in normal subject," *J. Amer. Soc. Echocardiogr.*, vol. 8, pp. 659–668, 1995.
- [20] J. Gorcsan, III, V. K. Gulati, W. A. Mandarino, and W. E. Katz, "Color-coded measures of myocardial velocity throughout the cardiac cycle by tissue Doppler imaging to quantify regional left ventricular function," *Amer. Heart J.*, vol. 131, no. 6, pp. 1203–1213, 1996.
- [21] G. R. Sutherland, G. D. Salvo, P. Claus, J. D'hooge, and B. Bijnens, "Strain and strain rate imaging: A new clinical approach to quantifying regional myocardial function," *J. Amer. Soc. Echocardiogr.*, vol. 17, no. 7, pp. 788–802, 2004.
- [22] H. Kanai, M. Sato, Y. Koiwa, and N. Chubachi, "Transcutaneous measurement and spectrum analysis of heart wall vibrations," *IEEE Trans. Ultrason., Ferroelect., Freq. Contr.*, vol. 43, no. 5, pp. 791–810, 1996.
- [23] H. Kanai, H. Hasegawa, N. Chubachi, Y. Koiwa, and M. Tanaka, "Noninvasive evaluation of local myocardial thickening and its color-coded imaging," *IEEE Trans. Ultrason., Ferroelect., Freq. Contr.*, vol. 44, no. 4, pp. 752–768, 1997.
- [24] H. Kanai and Y. Koiwa, "Myocardial rapid velocity distribution," *Ultrasound Med. Biol.*, vol. 27, no. 4, pp. 481–498, 2001.
- [25] F. Jamal, T. Kukulski, J. Strotmann, M. Szilard, J. D'hooge, B. Bijnens, F. Rademakers, L. Hatle, I. D. Scheerder, and G. R. Sutherland, "Quantification of the spectrum of changes in regional myocardial function during acute ischemia in closed chest pigs: An ultrasonic strain rate and strain study," *J. Amer. Soc. Echocardiogr.*, vol. 14, no. 9, pp. 874–885, 2001.
- [26] H. Kanai, Y. Koiwa, and J. Zhang, "Real-time measurements of local myocardium motion and arterial wall thickening," *IEEE Trans. Ultrason., Ferroelect., Freq. Contr.*, vol. 46, no. 5, pp. 1229–1241, 1999.
- [27] H. Kanai, S. Yonechi, I. Susukida, Y. Koiwa, H. Kamada, and M. Tanaka, "Onset of pulsatile waves in the heart walls at end-systole," *Ultrasonics*, vol. 38, no. 1, pp. 405–411, 2000.
- [28] B. A. Auld, *Acoustic Fields and Waves in Solids*. 2nd ed. vol. II, Malabar, FL: Krieger, 1990, pp. 63–220.
- [29] H. F. Tiersten, *Linear Piezoelectric Plate Vibrations*. New York: Plenum, 1969, pp. 95–118.
- [30] I. A. Viktorov, *Rayleigh and Lamb Waves*. New York: Plenum, 1967, pp. 67–121.
- [31] T. Kundo, *Ultrasonic Nondestructive Evaluation*. New York: CRC Press, 2003, pp. 223–310.
- [32] H. L. Oestreicher, "Field and impedance of an oscillating sphere in a viscoelastic medium with an application to biophysics," *J. Acoust. Soc. Amer.*, vol. 23, no. 6, pp. 707–714, 1951.
- [33] S. D. Nikolic, K. Tamura, T. Tamura, M. Dahm, R. W. M. Frater, and E. L. Yellin, "Diastolic viscous properties of the intact canine left ventricle," *Circ. Res.*, vol. 67, no. 2, pp. 352–359, 1990.
- [34] L. Loeffler, III and K. Sagawa, "A one-dimensional viscoelastic model of cat heart muscle studied by small length perturbations during isometric contraction," *Circ. Res.*, vol. 36, no. 4, pp. 498–512, 1975.
- [35] L. B. Katsnelson, L. V. Nikitina, D. Chemla, O. Solovyova, C. Coirault, Y. Lecarpentier, and V. S. Markhasin, "Influence of viscosity on myocardium mechanical activity: A mathematical model," *J. Theoretical Biol.*, vol. 230, no. 3, pp. 385–405, 2004.
- [36] L. A. Frizzell, E. L. Carstensen, and J. F. Dyro, "Shear properties of mammalian tissues at low megahertz frequencies," *J. Acoust. Soc. Amer.*, vol. 60, no. 6, pp. 1409–1411, 1976.
- [37] E. L. Madsen, H. J. Sathoff, and J. A. Zagzebski, "Ultrasonic shear wave properties of soft tissues and tissue-like materials," *J. Acoust. Soc. Amer.*, vol. 74, no. 5, pp. 1346–1355, 1983.
- [38] B. K. Hoffmeister, S. E. Gehr, and J. G. Miller, "Anisotropy of the transverse mode ultrasonic properties of fixed tendon and fixed myocardium," *J. Acoust. Soc. Amer.*, vol. 99, no. 6, pp. 3826–3836, 1996.
- [39] Y. Onodera and P.-K. Choi, "Surface-wave modes on soft gels," *J. Acoust. Soc. Amer.*, vol. 104, no. 6, pp. 3358–3363, 1998.
- [40] P.-K. Choi, H. Takahashi, and Y. Onodera, "Determination of shear elasticity of fibrous soft tissues using surface waves," *IE-ICE Trans.*, vol. J84-A, no. 12, pp. 1439–1443, 2001. (in Japanese)
- [41] G. H. Templeton and L. R. Nardizzi, "Elastic and viscous stiffness of the canine left ventricle," *J. Appl. Physiol.*, vol. 36, no. 1, pp. 123–127, 1974.
- [42] B. M. Learoyd and M. G. Taylor, "Alterations with age in the viscoelastic properties of human arterial walls," *Circ. Res.*, vol. 18, no. 3, pp. 278–292, 1966.
- [43] B. S. Gow and M. G. Taylor, "Measurement of viscoelastic properties of arteries in the living dog," *Circ. Res.*, vol. 23, no. 1, pp. 111–122, 1968.
- [44] S. Nasseri, L. E. Bilston, and N. Phan-Thien, "Viscoelastic properties of pig kidney in shear, experimental results and modelling," *Rheol. Acta*, vol. 41, pp. 180–192, 2002.
- [45] E. R. Fitzgerald, E. Ackerman, and J. W. Fitzgerald, "Preliminary measurement of the viscoelastic properties of animal tissues at audio-frequencies," *J. Acoust. Soc. Amer.*, vol. 29, no. 1, pp. 61–64, 1957.
- [46] E. D. Verdonk, S. A. Wickline, and J. G. Miller, "Anisotropy of ultrasonic velocity and elastic properties in normal human myocardium," *J. Acoust. Soc. Amer.*, vol. 92, no. 6, pp. 3039–3050, 1992.
- [47] M. I. Noble, "The diastolic viscous properties of cat papillary muscle," *Circ. Res.*, vol. 40, no. 3, pp. 288–292, 1977.
- [48] W. Philippoff, "Viscoelasticity of polymer solutions at high pressures and ultrasonic frequencies," *J. Appl. Phys.*, vol. 34, no. 5, pp. 1507–1511, 1963.
- [49] T. A. Litovitz and E. H. Carnevale, "Effect of pressure on ultrasonic relaxation in liquids. II," *J. Acoust. Soc. Amer.*, vol. 30, no. 2, pp. 134–136, 1958.
- [50] T. L. Szabo, "A model for longitudinal and shear wave propagation in viscoelastic media," *J. Acoust. Soc. Amer.*, vol. 107, no. 5, pp. 2437–2446, 2000.
- [51] E. R. Fitzgerald, "Dynamic mechanical measurements during the lift to death transition in animal tissues," *Biorheology*, vol. 12, pp. 397–408, 1975.

- [52] M. Kulke, S. Fujita-Becker, E. Rostkova, C. Neagoe, D. Labeit, D. J. Manstein, M. Gautel, and W. A. Linke, "Interaction between PEVK-titin and actin filaments, origin of a viscous force component in cardiac myofibrils," *Circ. Res.*, vol. 89, no. 10, pp. 874–881, 2001.
- [53] J. G. Pinto and P. J. Patitucci, "Visco-elasticity of passive cardiac muscle," *Trans. ASME, J. Biomechan. Eng.*, vol. 102, no. 2, pp. 57–61, 1980.
- [54] T. J. Fraitas, Jr., A. Saeki, and D. A. Kass, "Effect of altering filling pattern on diastolic pressure-volume curve," *Circulation*, vol. 96, pp. 4408–4414, 1997.
- [55] S. R. Solomon and S. A. Glantz, "Regional ischemia increases sensitivity of left ventricular relaxation to volume in pigs," *Amer. J. Physiol.*, vol. 276, pp. H1994–H2005, 1999.



Hiroshi Kanai (M'89) was born in Matsumoto, Japan, on November 29, 1958. He received a B.E. degree in Electrical Communications from Tohoku University, Sendai, Japan, in 1981, and M.E. and Ph.D. degrees, also from Tohoku University, in 1983 and in 1986, both in electrical engineering.

From 1986 to 1988 he was with the Education Center for Information Processing, Tohoku University, as a research associate. From 1990 to 1992 he was a lecturer in the Department of Electrical Engineering, Faculty of Engineering, Tohoku University. From 1992 to 2001 he was an associate professor in the Department of Electrical Engineering, Faculty of Engineering, Tohoku University. Since 2001 he has been a professor in the Department of Electronic Engineering, Graduate School of Engineering, Tohoku University.

His present interests are in ultrasonic measurement and digital signal processing for diagnosis of heart diseases and arteriosclerosis.

Dr. Kanai is a member of IEEE, the Acoustical Society of Japan, the Institute of Electronics Information and Communication Engineering of Japan, the Japan Society of Mechanical Engineers, the Japan Society of Ultrasonics in Medicine, the Japan Society of Medical Electronics and Biological Engineering, and the Japanese Circulation Society.